Cryo-EM structure of the human neutral amino acid transporter ASCT2

Alisa A. Garaeva[1], Gert T. Oostergetel[2], Cornelius Gati[3,4], Albert Guskov[2*], Cristina Paulino[2*] and Dirk J. Slotboom[1,5*]

Human ASCT2 belongs to the SLC1 family of secondary transporters and is specific for the transport of small neutral amino acids. ASCT2 is upregulated in cancer cells and serves as the receptor for many retroviruses; hence, it has importance as a potential drug target. Here we used single-particle cryo-EM to determine a structure of the functional and unmodified human ASCT2 at 3.85-Å resolution. ASCT2 forms a homotrimeric complex in which each subunit contains a transport and a scaffold domain. Prominent extracellular extensions on the scaffold domain form the predicted docking site for retroviruses. Relative to structures of other SLC1 members, ASCT2 is in the most extreme inward-oriented state, with the transport domain largely detached from the central scaffold domain on the cytoplasmic side. This domain detachment may be required for substrate binding and release on the intracellular side of the membrane.

The solute carrier 1 (SLC1) family of secondary membrane transporters includes seven human members: the glutamate transporters EAAT1–EAAT5 and the neutral amino acid transporters ASCT1 and ASCT2 (refs [1,2] and Supplementary Note). Glutamate transporters are expressed in glia and neurons and use membrane gradients of Na^+, K^+ and protons to pump the neurotransmitter L-glutamate from the extracellular fluid into the cytoplasm, thereby preventing neurotoxicity[3,4]. EAAT proteins are also expressed outside the central nervous system in various tissues, where they are involved in intercellular glutamate signaling and are linked to glutamine synthesis pathways[5]. ASCT proteins reside in the plasma membranes of many cell types. They function as sodium-dependent obligate exchangers of neutral amino acids such as serine, alanine and threonine, but their precise physiological roles are not fully understood[1]. ASCT2 is present mainly outside the central nervous system, where it is assumed to contribute to glutamine homeostasis[6]. ASCT2 is upregulated in several cancer types, such as melanoma, lung, prostate and breast cancer, in which it presumably manages the increased demand of cancer cells for glutamine[7–15]. In addition to its role as a transporter, ASCT2 is also a receptor for many retroviruses, including simian retrovirus 4, feline endogenous virus, human endogenous retrovirus type W and baboon M7 endogenous virus[16–19].

Several crystal structures of the prokaryotic SLC1 transporters Glt_{Ph} (refs [20–22]) and Glt_{Tk} (refs [23,24]), as well as an engineered version of human EAAT1 (ref. [25]), have been determined. All these proteins form homotrimers in which each protomer consists of a scaffold domain and a transport domain. The scaffold domains form a stable central assembly, whereas the transport domains are located at the periphery of the complex and bind the transported substrate and coupled cations. Multiple conformations observed in crystal structures (reviewed in ref. [26]) have revealed large differences in the relative orientations of the scaffold and transport domains. The interconversion between the conformational states brings the substrate from one side of the membrane to the other, and the transport mechanism has been compared to an elevator. Two structural elements (helical hairpins 1 and 2 (HP1 and HP2)), which occlude the substrate during transport, have been proposed to act as gates that allow access to the binding site from the cytoplasmic and extracellular sides of the membrane, respectively[20,22,27]. The crystal structures have provided major insight into the transport mode of glutamate transporters, but without structural information on ASCT2, the differences in substrate specificity and transport modes between ASCT2 and EAAT proteins (amino acid exchange by ASCT2 and concentrative uptake by EAATs) remain unexplained. In addition, the lack of structural information on ASCT2 makes the mechanism by which retroviruses interact with the protein unclear and hampers the design of potential anticancer drugs targeting ASCT2. Here, we present a single-particle cryo-EM structure of the functional and unmodified human transport protein ASCT2.

Results

Transport activity of ASCT2 in proteoliposomes. We produced human ASCT2 in the yeast *Pichia pastoris* by expression of genome-integrated *ASCT2* (official symbol *SLC1A5*) (ref. [28]), and purified the protein by using a C-terminal hexahistidine tag. Recent work[29] has suggested that ASCT2 purified from this expression strain catalyzes electrogenic amino acid exchange, a function inconsistent with electrophysiological data from various laboratories showing an electroneutral exchange[30–33]. To resolve this apparent discrepancy, we reconstituted purified ASCT2 into proteoliposomes and studied glutamine transport (Fig. 1). Proteoliposomes loaded with 10 mM unlabeled glutamine showed robust exchange with external radiolabeled [^{3}H]glutamine (Fig. 1), whereas proteoliposomes without lumenal amino acid did not support transport (Fig. 1c,d). Transport was strictly dependent on sodium ions but was not affected by the transmembrane voltage generated by valinomycin-mediated potassium diffusion (Fig. 1e). Thus, we conclude that amino acid exchange by human ASCT2 in proteoliposomes is electroneutral, in agreement with the electrophysiological data. The substrate specificity

[1]University of Groningen, Groningen Biomolecular Sciences and Biotechnology Institute, Membrane Enzymology, Groningen, the Netherlands. [2]University of Groningen, Groningen Biomolecular Sciences and Biotechnology Institute, Structural Biology, Groningen, the Netherlands. [3]SLAC National Accelerator Laboratory, Bioscience Division, Menlo Park, CA, USA. [4]Stanford University, Department of Structural Biology, Stanford, CA, USA. [5]University of Groningen, Zernike Institute for Advanced Materials, Groningen, the Netherlands. *e-mail: a.guskov@rug.nl; c.paulino@rug.nl; d.j.slotboom@rug.nl

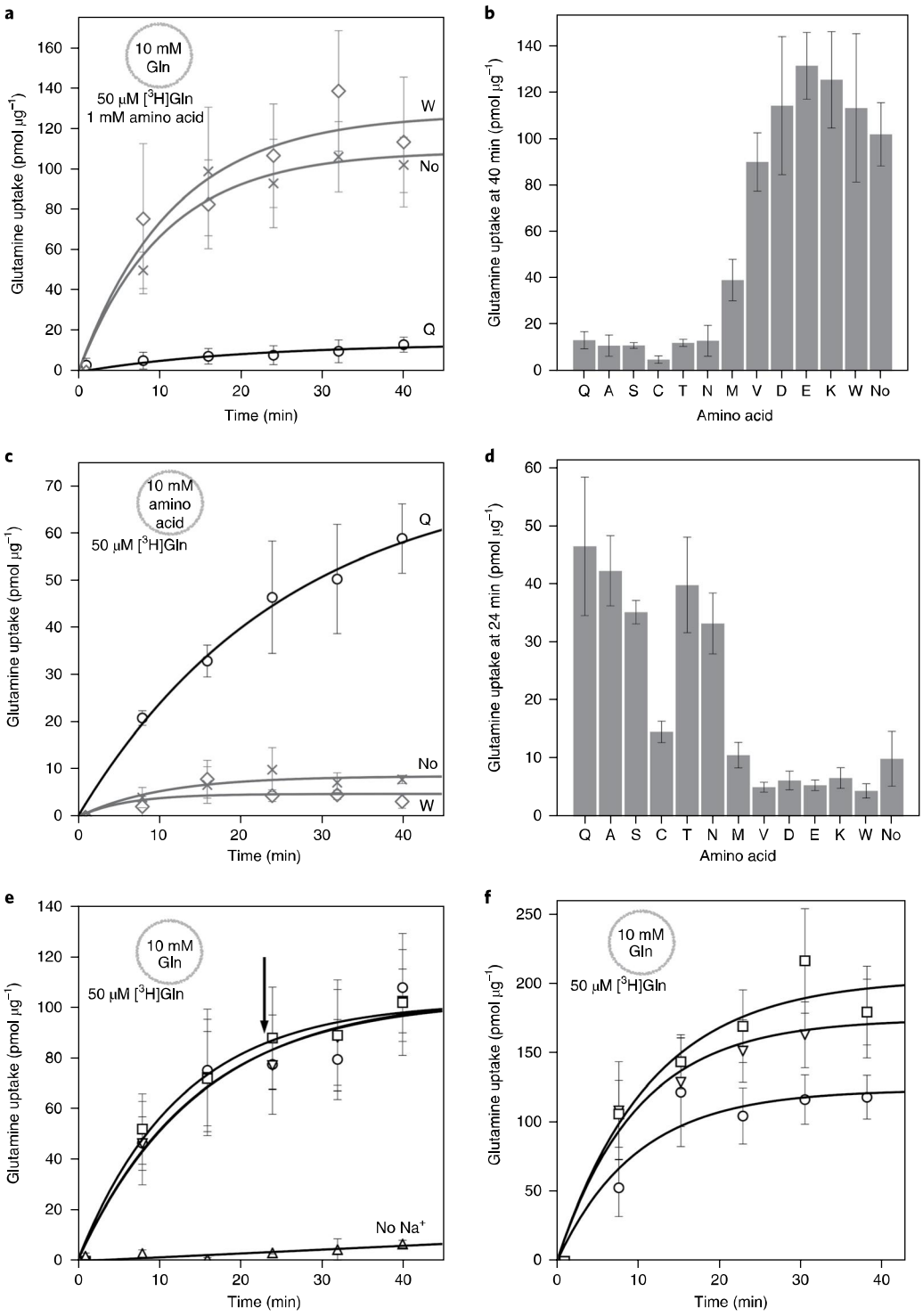

Fig. 1 | Functional characterization of ASCT2. a, Exchange of internal unlabeled glutamine with external [^{3}H]glutamine, and inhibition of transport by addition of an excess of unlabeled amino acids (circle, glutamine; diamond, tryptophan; X, no externally added amino acid (No)). **b**, Inhibitory effect of externally added amino acids. **c**, Exchange of internal amino acid substrate. **d**, Ability of alternative internal amino acids to drive uptake of glutamine. **e**, Electroneutral nature of exchange and sodium dependency. Circle, 3 μM valinomycin was added at 23 min to proteoliposomes with a 100-fold K^+ gradient; downward triangle, ethanol was added at 23 min to proteoliposomes with a 100-fold K^+ gradient; square, 3 μM valinomycin was added at the start to proteoliposomes with a 100-fold K^+ gradient; upward triangle, proteoliposomes in the absence of Na^+. Arrow indicates time of addition of valinomycin or ethanol (23 min). **f**, Exchange of internal unlabeled glutamine with external [^{3}H]glutamine in proteoliposomes containing different amounts of cholesterol. Circle, proteoliposomes without cholesterol; downward triangle, with 5% (wt/wt) cholesterol; square, with 10% (wt/wt) cholesterol. Data points and error bars represent means ± s.e.m. from 3 biologically independent experiments, each done in one technical replicate. Small schemes in the top left corners of **a**, **c**, **e** and **f** schematically represent proteoliposomes with internal and external compound compositions used in corresponding experiments.

(Fig. 1a–d), and the apparent K_m values for glutamine (56 ± 3.9 μM) and sodium (16.5 ± 3.5 mM) determined with our preparations also match those reported for ASCT2 expressed in oocytes and HEK 293 cells[30,32,33], thus indicating that the human ASCT2 purified from *P. pastoris* was appropriate for structural analysis.

Structure determination and overall fold. We used single-particle cryo-EM to solve a structure of ASCT2 in micelles of *n*-dodecyl-β-D-maltopyranoside (DDM) and cholesterol hemisuccinate (CHS) at 3.85-Å resolution (Table 1, Supplementary Figs. 1 and 2, and Supplementary Video 1). The inclusion of CHS with the detergent-solubilized protein was essential to obtaining homogeneous protein preparations. The stability of the purified protein was further enhanced by the inclusion of 1 mM of the substrate glutamine in all buffers used for purification. The transport activity of ASCT2 was higher in the presence of 5–10% (wt/wt) cholesterol in proteoliposomes (Fig. 1f), thus indicating that cholesterol did not stabilize the protein by locking it in an inactive state. The cryo-EM density allowed us to build a model of the entire protein, with the exception of the extreme N and C termini, and 15 residues of the loop between transmembrane segments (TMs) 3 and 4 (Supplementary Fig. 2 and Supplementary Video 1). The overall trimeric organization of the protein resembles that of EAAT1 (ref. [25]), Glt_{Ph} (ref. [20]) and Glt_{Tk} (ref. [24]). Each protomer contains a scaffold domain (TMs 1, 2, 4 and 5) that mediates all interactions between the protomers, and a transport domain consisting of TMs 3, 6, 7 and 8 and the two helical hairpins predicted to act as gates (HP1 between TMs 6 and 7, and HP2 between TMs 7 and 8) (Fig. 2, Supplementary Note and Supplementary Fig. 3a,b).

Table 1 | Cryo-EM data collection, refinement and validation statistics

	ASCT2 (EMD-4386, PDB 6GCT)
Data collection and processing	
Magnification	49,407
Voltage (kV)	200
Electron exposure (e^-/Å^2)	52
Defocus range (μm)	−0.4 to −2.5
Pixel size (Å)	1.012
Symmetry imposed	C3
Initial particle images (no.)	628,015
Final particle images (no.)	133,437
Map resolution (Å)	3.85
FSC threshold	0.143
Map resolution range (Å)	3.7–5.3
Refinement	
Initial model used	PDB 3KBC
Model resolution (Å)	3.9
FSC threshold	0.5
Model resolution range (Å)	
Map-sharpening *B* factor (Å^2)	−171
Model composition	
Nonhydrogen atoms	9,672
Protein residues	1,296
Ligands	3
B factors (Å^2)	
Protein	49.7
Ligand	52.3
R.m.s. deviations	
Bond lengths (Å)	0.012
Bond angles (°)	1.369
Validation	
MolProbity score	2.35
Clashscore	6.85
Poor rotamers (%)	5.57
Ramachandran plot	
Favored (%)	93.93
Allowed (%)	5.84
Disallowed (%)	0.23

Retroviral docking site. TM4 of the scaffold domain contains a stretch of 28 amino acids between helical segments TM4b and TM4c, which is highly diverse in different SLC1 members (both in length and in amino acid sequence; Supplementary Note). The additional segment consists of an extended amino acid stretch (resembling a β-strand) that is directed outward toward the extracellular space, a turn and a second extended stretch that brings the sequence back to the protein core (Fig. 2a–c). The three segments (one from each protomer) protrude from the proteins similarly to antennae, with their bases located in a conserved bowl-shaped indentation around the three-fold symmetry axis at the outer surface of the protein[20]. In the outward-oriented states observed for EAAT1 and prokaryotic SLC1 members, this bowl provides access to the substrate-binding site[20,21,25]. Despite the presence of the antennae in ASCT2, there is sufficient space left for substrate molecules to diffuse into the aqueous bowl to a similar depth as in EAAT1, Glt_{Ph} and Glt_{Tk} (Fig. 2c). Asn212, located close to the tip of the antenna, is glycosylated when the protein is expressed in HEK 293 cells[34]. We did not observe density for the sugar residues, a result consistent with the lack of glycosylation when the protein was expressed in *P. pastoris*. The three outward-facing antennae with possible glycosylation at the tip create a characteristic extracellular surface on the protein, which is likely to be the docking site for retroviruses that have been shown to use ASCT2 as a cellular receptor for internalization. This hypothesis is consistent with the observation that differences in the loop sequence confer differences in virus specificity[35].

Glutamine-binding site. When superimposed separately, the structures of the transport domains of EAAT1 and ASCT2 are very similar (r.m.s. deviation ~1 Å, 50% sequence identity; Supplementary Fig. 3a,b)—a remarkable result, given the different substrate specificities and transport modes. Not only the overall fold of the domains but also most of the binding-site residues are conserved (Fig. 3a), except for only Cys467 (TM8) and Ala390 (TM7) in ASCT2. In EAATs, an arginine residue invariably occupies the position occupied by Cys467 in ASCT2 and interacts with the acidic side chain of the substrate glutamate[25]. Mutation of the arginine into cysteine renders the rabbit glutamate transporter EAAC1 (EAAT3) specific to neutral amino acids rather than glutamate[36] and similarly allows Glt_{Ph} to accept serine and alanine as substrates[37]. These observations are consistent with a role of Cys467 as the main determinant of selectivity for neutral amino acid substrates in ASCT2. The position of Ala390 is occupied by a threonine residue in all concentrative glutamate and aspartate transporters (Supplementary Note). This threonine residue has been proposed to allosterically couple Na^+ and substrate binding[23], thus increasing the apparent affinity for the amino acid at high (external) Na^+ concentration and decreasing the affinity at the lower intracellular concentration of the cation. The allosteric modulation may not be necessary in ASCT2, because the protein catalyzes amino acid exchange rather than accumulation.

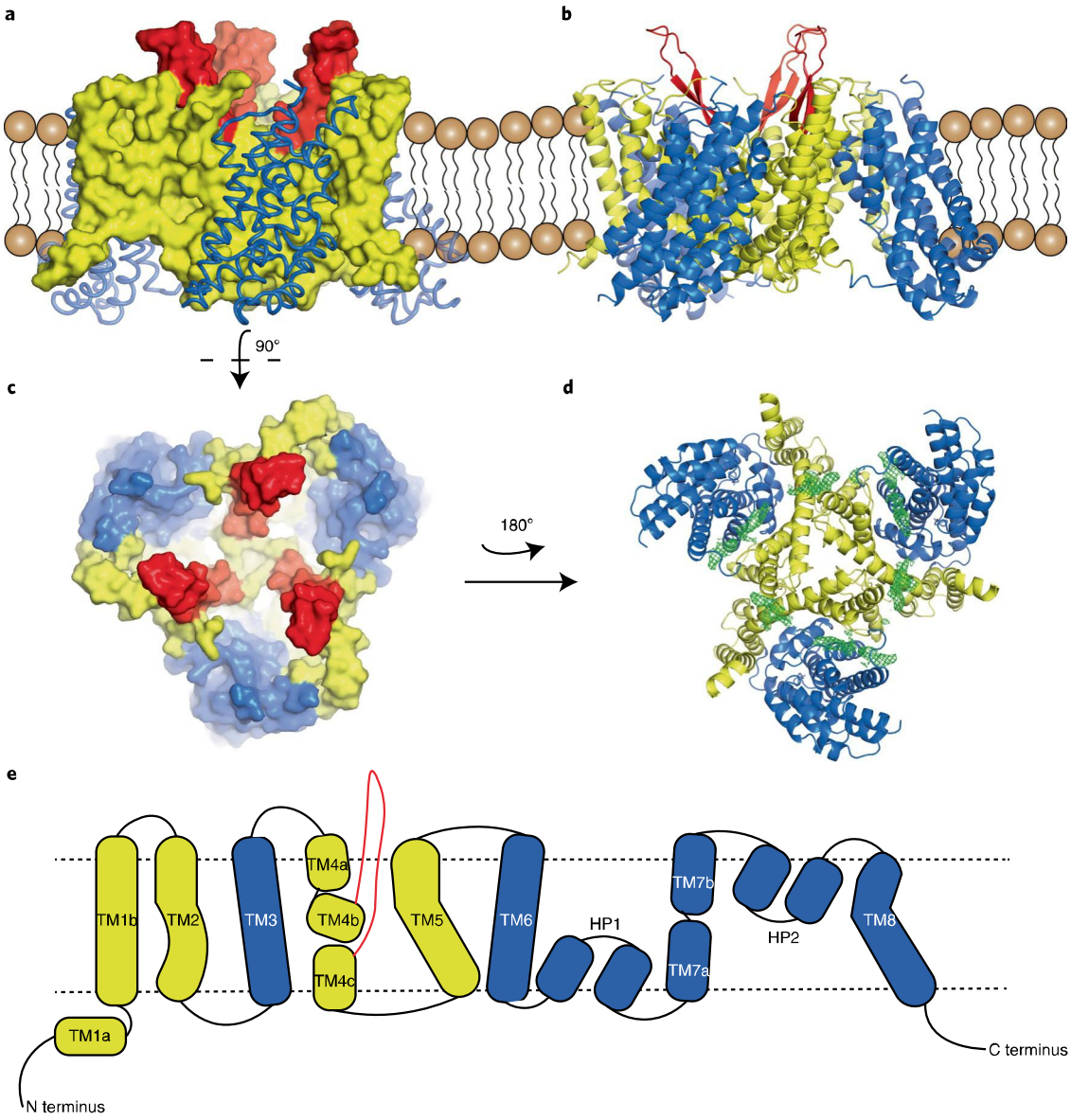

Fig. 2 | Structural model of ASCT2. a, Side view with the scaffold domains as yellow surface; the protruding loops serving as a docking area for retroviruses as red surface; and the transport domains as blue ribbon. **b**, Side view, showing a large gap between the scaffold and transport domains. **c**, Top view: the protruding loops (red) do not block the access of the deep indentations for substrate. **d**, Bottom view: extra patches of density (green mesh) are observed between the scaffold and transport domains. Additional data in Supplementary Fig. 4e. **e**, Membrane topology of ASCT2: transmembrane segments and hairpins are labeled and color coded as in a–d.

Orientation of the transport domain relative to the scaffold domain. Notwithstanding the similarity in their structures, the transport domains of EAAT1 and ASCT2 adopt very different orientations relative to the scaffold domain (Fig. 3c,d, Supplementary Fig. 3c,d and Supplementary Video 2). The transport domain is in an outward-oriented substrate-occluded state in EAAT1, whereas it is in an inward-oriented state in ASCT2. Notably, despite the large initial cryo-EM dataset and extensive 3D classifications, we did not find the transporter in a different state in our samples, thus indicating that our structure represents the preferred state in our homogeneous protein preparations (Supplementary Fig. 1e). The interface between the scaffold and transport domains buries a surface of ~1,300 Å^2, which is smaller than the buried surfaces observed in the crystal structures of EAAT1, Glt_{Ph} and Glt_{Tk} in outward-facing states, as well as in the structure of prokaryotic Glt_{Ph} in an inward-facing state (~2,100 Å^2, ~1,850 Å^2, ~1,630 Å^2 and ~1,600 Å^2, respectively). However, it is larger than the interaction surface (~1,000 Å^2) observed in the unlocked mutant of Glt_{Ph}[38] (visualization of the interfaces in Supplementary Fig. 4a–d). In ASCT2, the contacts between the scaffold domain and the transport domain are located exclusively near the extracellular side of the membrane. In the transport domain, the only residues involved in the domain contacts are located at the N-terminal end of TM8 and the base of HP2 (Fig. 3d and Supplementary Video 2). Among the few residue pairs at the interface are Arg101 of the scaffold domain and Glu444 at the C-terminal end of HP2, which may stabilize the inward state by forming a salt bridge (Fig. 3b). EAATs contain a serine or threonine residue at the equivalent position of Glu444. Therefore, a similar salt bridge cannot be formed in these proteins, which might contribute to the adoption of the outward-oriented state in the crystal

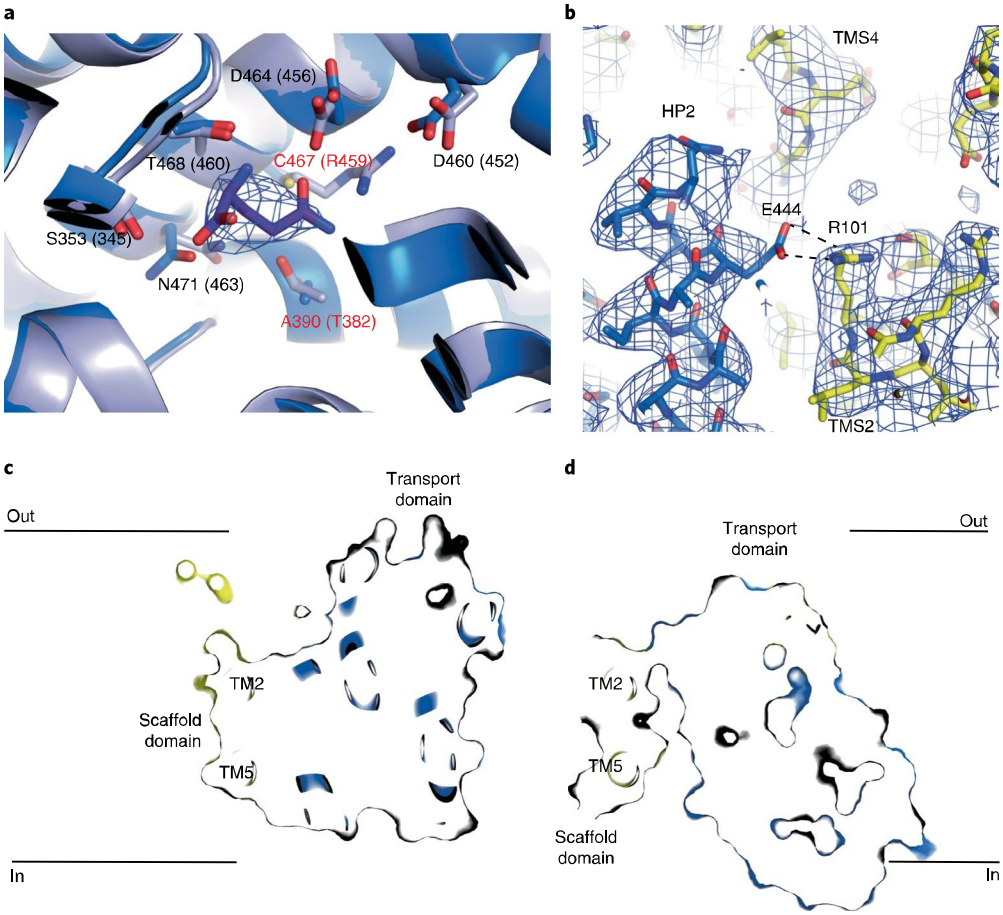

Fig. 3 | Domain and substrate interactions within ASCT2. a, Superposition of the substrate-binding sites from ASCT2 (bright blue) and EAAT1 (pale blue). The residues are numbered according to the ASCT2 sequence (numbering for EAAT1 is in parentheses), and those that differ between the two proteins are highlighted in red. The bound glutamine (to ASCT2) is shown as dark purple sticks, and the corresponding density is shown as blue mesh at 4σ. **b**, Potential salt bridge formed between the transport (blue) and scaffold (yellow) domains. Density is shown as blue mesh at 5σ. **c**,**d**, Slice-through views from the membrane plane of the interface between scaffold and transport domains in EAAT1 (outward facing) and ASCT2 (inward facing), respectively. In ASCT2, the interface is much smaller, and a large gap between the domains is visible.

structures of EAAT1, although other factors, such as crystal packing, may also play a role. Notably, the surfaces of the transport and scaffold domains in EAAT1 and ASCT2 have similar overall shape and hydrophobicity, and therefore cannot explain the preference for different states in the two proteins.

Discussion

The inward-oriented state of ASCT2 is different from that found in crystal structures of Glt_{Ph} (refs. [22,38]). It is most similar to the conformation of a mutant of Glt_{Ph} with a modified interface between the scaffold and transport domain, which leads to detachment or 'unlocking' of the domains. In the structure of ASCT2, the transport domain is also largely detached from the scaffold domain (Figs. 2b and 3d), but it is located farther toward the cytoplasm, relative to its position in Glt_{Ph}, by a distance of ~4.5 Å, measured at the tip of HP2 (Supplementary Video 2). On the extracellular side of the membrane, the transport and scaffold domains are closer in ASCT2 than in the unlocked Glt_{Ph} mutant, and the base of HP2 swings toward the scaffold by ~7.5 Å compared with Glt_{Ph}. In contrast, on the cytoplasmic side of the membrane, the domains are farther apart, and the C-terminal end of TM6 and the base of HP1 move away from the scaffold by up to 10 Å when compared with unlocked Glt_{Ph} (Supplementary Fig. 4c and Supplementary Video 2). There is a gap between the two domains that is probably accessible to lipids. Indeed, we observed several unassigned patches of cryo-EM density between the scaffold and transport domains that may correspond to lipid molecules (Fig. 2d and Supplementary Fig. 4e), but the resolution of the map does not allow for unambiguous identification of the molecules. Lipids have been shown to regulate the activity of SLC1 proteins, and beside the proposed binding sites on surface crevices of the proteins, the structure of ASCT2 suggests that lipids can also diffuse into the space between the transport and scaffold domains. Molecular dynamics simulations on the unlocked Glt_{Ph} mutant also show that lipids can diffuse between the domains (ref. [38]). In addition, structures of the unrelated secondary transporters CitS and NapA also show that lipids may intercalate between the transport and scaffold domains (refs [39,40]), thus suggesting that lipid diffusion between the domains may be a more general feature of transporters that use elevator-type mechanisms.

The transport domains of glutamate transporters contain internal pseudosymmetry with inverted membrane topology, in which HP1 is related to HP2, TM6 is related to TM3, and TM7 is related to TM8 (refs [22,27,41]). Similar inverted topologies have been found in many transporters, and rotation around a two-fold axis parallel to the membrane plane has been used as a method to model the conformational changes associated with the movement between inward- and outward-facing states. A comparison of the orientations of the transport domains from EAAT1 and ASCT2 with the scaffold domains superimposed indicates an almost perfect pseudosymmetry when the domains are rotated around a two-fold axis

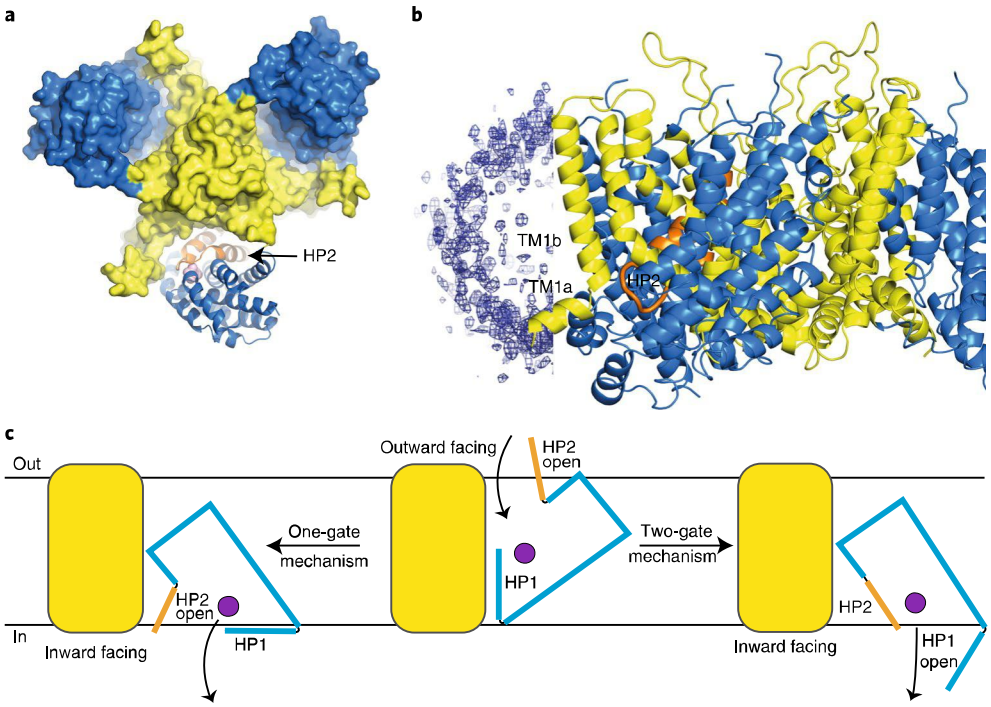

Fig. 4 | Position of HP2. a, ASCT2 view from the cytoplasm. One of the transport domains, shown as a cartoon with its HP2 colored orange. The tip of HP2 is detached from the scaffold domain. **b**, HP2 is located very close to the cytoplasm. The membrane/cytoplasm interface is defined by the position of surface helix TM1a and the density observed for the micelle. **c**, Schematic representation of the scaffold (in yellow) and transport (as outline) domains, HP2 in orange and the substrate as a purple circle. Two possibilities for gating in the inward-oriented state are indicated, with either HP2 (left, single-gate elevator) or HP1 (right, two-gate elevator) acting as a gate. Gate HP2 is open in the outward-facing orientation, as observed in the EAAT1 structure (middle).

in the membrane plane, thus suggesting that the two states may represent the extremes of inward and outward-facing conformations (Supplementary Fig. 5).

On the basis of the structural pseudosymmetry, the possibility that there may also be functional symmetry has also been proposed, with HP2 acting as an external gate, and HP1 acting as a gate on the cytoplasmic side (refs [22,27]). There is indeed support from crystal structures in the presence of the inhibitor TBOA that HP2 acts as a gate in the outward-facing state[21,25], but there is no experimental evidence for the hypothesis that HP1 acts as a gate in the inward-facing state. The position of the transport domain in ASCT2 suggests that a different mechanism of gating on the cytoplasmic side may be possible. In ASCT2, the tip of HP2 is located all the way on the cytoplasmic side of the membrane (Fig. 4a,b and Supplementary Video 2). Because it is not packed against the scaffold domain, HP2 in the inward-facing state might possibly open in a similar manner as has been shown for Glt_{Ph} and EAAT1 in the outward state. Therefore, a single gate might alternately allow access from both sides of the membrane, without the need for HP1 to open[38] (Fig. 4c). Such a scenario has also been hypothesized on the basis of the crystal structure of the unlocked Glt_{Ph} mutant protein. Further structural studies are necessary to test this hypothesis. An alternating-access mechanism of a mobile domain with a fully occluded substrate that combines large movements with a single gate would resemble the toppling mechanism observed in ECF-type ABC transporters[42]. In ECF transporters, the S subunit is the equivalent of the transport domain in the SLC1 transporters. It binds and occludes the substrate on the extracellular side of the membrane by using a gate formed by loops (as in the SLC1 transporters). The S component moves in the membrane as a rigid body relative to the second subunit (EcfT, the equivalent of the scaffold domain) and thus brings the substrate to the cytoplasmic side of the membrane, where it dissociates from the occluded binding site by using the same gate as on the extracellular site. This mechanism of transport is different from those of other secondary transporters that use elevator-like movements, such as CitS and NhaA. In these proteins, the substrates are not entirely occluded by the transport domain but instead move exposed along the interface between the transport and scaffold domains, without the use of loops as gates.

The structure of ASCT2 presented here provides a first glimpse of the structural features that serve as a docking domain for retroviruses, as well as new details on subtype-specific differences among human SLC1 members. In addition, the observed detachment of the transport domain from the scaffold domain indicates that an elevator-like transport mechanism with a single gate (HP2) may be possible. Nonetheless, important questions remain. For instance, the remarkable structural similarity between the transport domains of ASCT2 and EAAT1 makes explaining the pronounced differences in transport mode (obligate exchange and cation-driven accumulation, respectively) difficult. Apparently, subtle variations between the subtypes must prevent the apo state of ASCT2 from reorienting between inward- and outward-facing states. Further characterization is needed to elucidate the structural basis of mechanistic differences between EAATs and ASCT2.

References

1. Kanai, Y. et al. The SLC1 high-affinity glutamate and neutral amino acid transporter family. *Mol. Aspects Med.* **34**, 108–120 (2013).
2. Slotboom, D. J., Konings, W. N. & Lolkema, J. S. Structural features of the glutamate transporter family. *Microbiol. Mol. Biol. Rev.* **63**, 293–307 (1999).
3. Kanner, B. I. & Sharon, I. Active transport of L-glutamate by membrane vesicles isolated from rat brain. *Biochemistry* **17**, 3949–3953 (1978).
4. Zerangue, N. & Kavanaugh, M. P. Flux coupling in a neuronal glutamate transporter. *Nature* **383**, 634–637 (1996).
5. Danbolt, N. C. Glutamate uptake. *Prog. Neurobiol.* **65**, 1–105 (2001).
6. Pochini, L., Scalise, M., Galluccio, M. & Indiveri, C. Membrane transporters for the special amino acid glutamine: structure/function relationships and relevance to human health. *Front Chem.* **2**, 61 (2014).
7. Toda, K. et al. Clinical role of ASCT2 (SLC1A5) in KRAS-mutated colorectal cancer. *Int. J. Mol. Sci.* **18**, E1632 (2017).
8. Kaira, K. et al. Relationship between CD147 and expression of amino acid transporters (LAT1 and ASCT2) in patients with pancreatic cancer. *Am. J. Transl. Res.* **7**, 356–363 (2015).
9. Kim, S., Kim, D. H., Jung, W.-H. & Koo, J. S. Expression of glutamine metabolism-related proteins according to molecular subtype of breast cancer. *Endocr. Relat. Cancer* **20**, 339–348 (2013).
10. Shimizu, K. et al. ASC amino-acid transporter 2 (ASCT2) as a novel prognostic marker in non-small cell lung cancer. *Br. J. Cancer* **110**, 2030–2039 (2014).
11. Wang, Q. et al. Targeting ASCT2-mediated glutamine uptake blocks prostate cancer growth and tumour development. *J. Pathol.* **236**, 278–289 (2015).
12. Bode, B. P., Kaminski, D. L., Souba, W. W. & Li, A. P. Glutamine transport in isolated human hepatocytes and transformed liver cells. *Hepatology* **21**, 511–520 (1995).
13. Bröer, A., Rahimi, F. & Bröer, S. Deletion of amino acid transporter ASCT2 (SLC1A5) reveals an essential role for transporters SNAT1 (SLC38A1) and SNAT2 (SLC38A2) to sustain glutaminolysis in cancer cells. *J. Biol. Chem.* **291**, 13194–13205 (2016).
14. Wang, Q. et al. Targeting glutamine transport to suppress melanoma cell growth. *Int. J. Cancer* **135**, 1060–1071 (2014).
15. van Geldermalsen, M. et al. ASCT2/SLC1A5 controls glutamine uptake and tumour growth in triple-negative basal-like breast cancer. *Oncogene* **35**, 3201–3208 (2016).
16. Yoshikawa, R. et al. Simian retrovirus 4 induces lethal acute thrombocytopenia in Japanese macaques. *J. Virol.* **89**, 3965–3975 (2015).
17. Shimode, S., Nakaoka, R., Shogen, H. & Miyazawa, T. Characterization of feline ASCT1 and ASCT2 as RD-114 virus receptor. *J. Gen. Virol.* **94**, 1608–1612 (2013).
18. Tailor, C. S., Nouri, A., Zhao, Y., Takeuchi, Y. & Kabat, D. A sodium-dependent neutral-amino-acid transporter mediates infections of feline and baboon endogenous retroviruses and simian type D retroviruses. *J. Virol.* **73**, 4470–4474 (1999).
19. Lavillette, D. et al. The envelope glycoprotein of human endogenous retrovirus type W uses a divergent family of amino acid transporters/cell surface receptors. *J. Virol.* **76**, 6442–6452 (2002).
20. Yernool, D., Boudker, O., Jin, Y. & Gouaux, E. Structure of a glutamate transporter homologue from *Pyrococcus horikoshii*. *Nature* **431**, 811–818 (2004).
21. Boudker, O., Ryan, R. M., Yernool, D., Shimamoto, K. & Gouaux, E. Coupling substrate and ion binding to extracellular gate of a sodium-dependent aspartate transporter. *Nature* **445**, 387–393 (2007).
22. Reyes, N., Ginter, C. & Boudker, O. Transport mechanism of a bacterial homologue of glutamate transporters. *Nature* **462**, 880–885 (2009).
23. Guskov, A., Jensen, S., Faustino, I., Marrink, S. J. & Slotboom, D. J. Coupled binding mechanism of three sodium ions and aspartate in the glutamate transporter homologue Glt_{Tk}. *Nat. Commun.* **7**, 13420 (2016).
24. Jensen, S., Guskov, A., Rempel, S., Hänelt, I. & Slotboom, D. J. Crystal structure of a substrate-free aspartate transporter. *Nat. Struct. Mol. Biol.* **20**, 1224–1226 (2013).
25. Canul-Tec, J. C. et al. Structure and allosteric inhibition of excitatory amino acid transporter 1. *Nature* **544**, 446–451 (2017).
26. Arkhipova, V., Guskov, A. & Slotboom, D. J. Analysis of the quality of crystallographic data and the limitations of structural models. *J. Gen. Physiol.* **149**, 1091–1103 (2017).
27. Crisman, T. J., Qu, S., Kanner, B. I. & Forrest, L. R. Inward-facing conformation of glutamate transporters as revealed by their inverted-topology structural repeats. *Proc. Natl Acad. Sci. USA* **106**, 20752–20757 (2009).
28. Pingitore, P. et al. Large scale production of the active human ASCT2 (SLC1A5) transporter in *Pichia pastoris*: functional and kinetic asymmetry revealed in proteoliposomes. *Biochim. Biophys. Acta* **1828**, 2238–2246 (2013).
29. Scalise, M. et al. Transport mechanism and regulatory properties of the human amino acid transporter ASCT2 (SLC1A5). *Amino Acids* **46**, 2463–2475 (2014).
30. Bröer, A., Wagner, C., Lang, F. & Bröer, S. Neutral amino acid transporter ASCT2 displays substrate-induced Na^+ exchange and a substrate-gated anion conductance. *Biochem. J.* **346**, 705–710 (2000).
31. Bröer, A. et al. The astroglial ASCT2 amino acid transporter as a mediator of glutamine efflux. *J. Neurochem.* **73**, 2184–2194 (1999).
32. Utsunomiya-Tate, N., Endou, H. & Kanai, Y. Cloning and functional characterization of a system ASC-like Na^+-dependent neutral amino acid transporter. *J. Biol. Chem.* **271**, 14883–14890 (1996).
33. Zander, C. B., Albers, T. & Grewer, C. Voltage-dependent processes in the electroneutral amino acid exchanger ASCT2. *J. Gen. Physiol.* **141**, 659–672 (2013).
34. Console, L., Scalise, M., Tarmakova, Z., Coe, I. R. & Indiveri, C. N-linked glycosylation of human SLC1A5 (ASCT2) transporter is critical for trafficking to membrane. *Biochim. Biophys. Acta* **1853**, 1636–1645 (2015).
35. Marin, M., Lavillette, D., Kelly, S. M. & Kabat, D. N-linked glycosylation and sequence changes in a critical negative control region of the ASCT1 and ASCT2 neutral amino acid transporters determine their retroviral receptor functions. *J. Virol.* 77, 2936–2945 (2003).
36. Bendahan, A., Armon, A., Madani, N., Kavanaugh, M. P. & Kanner, B. I. Arginine 447 plays a pivotal role in substrate interactions in a neuronal glutamate transporter. *J. Biol. Chem.* **275**, 37436–37442 (2000).
37. Scopelliti, A. J., Font, J., Vandenberg, R. J., Boudker, O. & Ryan, R. M. Structural characterisation reveals insights into substrate recognition by the glutamine transporter ASCT2/SLC1A5. *Nat. Commun.* **9**, 38 (2018).
38. Akyuz, N. et al. Transport domain unlocking sets the uptake rate of an aspartate transporter. *Nature* **518**, 68–73 (2015).
39. Wöhlert, D., Grötzinger, M. J., Kühlbrandt, W. & Yildiz, Ö. Mechanism of Na^+-dependent citrate transport from the structure of an asymmetrical CitS dimer. *eLife* **4**, e09375 (2015).
40. Coincon, M. et al. Crystal structures reveal the molecular basis of ion translocation in sodium/proton antiporters. *Nat. Struct. Mol. Biol.* **23**, 248–255 (2016).
41. Drew, D. & Boudker, O. Shared molecular mechanisms of membrane transporters. *Annu. Rev. Biochem.* **85**, 543–572 (2016).
42. Swier, L. J. Y. M., Guskov, A. & Slotboom, D. J. Structural insight in the toppling mechanism of an energy-coupling factor transporter. *Nat. Commun.* **7**, 11072 (2016).

Acknowledgements

We thank C. Indivieri (Università della Calabria, Italy) for kindly providing the *P. pastoris* expression strain, R.C. Prins for her help in preparation of cholesterol-containing proteoliposomes, M. Punter for help in setting up the image-processing cluster and B. Poolman for critical reading and discussion of the manuscript. This research was supported by NWO Vidi grant 723.014.002 to A.G.; NWO Veni grant 722.017.001 and Marie Skłodowska–Curie Individual Fellowship 749732 to C.P.; and NWO Vici grant 865.11.001 and European Research Council Starting Grant 282083 to D.J.S. C.G. thanks the SLAC National Accelerator Laboratory for financial support as part of the Panofsky fellowship program.

Author contributions

A.G. conceived the project. Expression, purification and transport assays were performed by A.A.G. Initial cryo-EM experiments were carried out by C.G. Further and final cryo-EM sample preparation and data collection was done by A.A.G., G.T.O. and C.P. Cryo-EM image processing was carried out by A.A.G. and C.P. Model building and refinement were done by A.G. D.J.S. supervised the project at all stages and wrote the manuscript with input from all other authors.

Competing interests

The authors declare no competing interests.

Correspondence and requests for materials should be addressed to A.G. or C.P. or D.J.S.

Publisher's note: Springer Nature remains neutral with regard to jurisdictional claims in published maps and institutional affiliations.

Methods

Expression and purification. ASCT2 was expressed in a strain of *P. pastoris* containing the genome-integrated human *ASCT2* gene, as previously described[28]. After expression, cells were harvested by centrifugation (15 min, 7,446 *g*, 4 °C), washed with buffer A (50 mM Tris-HCl, pH 7.4, and 150 mM NaCl), resuspended in the same buffer and flash frozen in liquid nitrogen. Cells were stored at −80 °C. Before disruption, 3 mM $MgCl_2$ and 0.1 mg ml^{-1} DNase A (Sigma-Aldrich) were added to the thawed cells. Cells were broken in three passages at 39 kPsi, 5 °C with a Constant Cell Disruption System. After the last passage, 1 mM PMSF was added to the cell lysate, which was subsequently centrifuged (30 min, 12,074 *g*, 4 °C) to remove cell debris. The membrane fraction was collected by ultracentrifugation of the supernatant (120 min, 193,727 *g*, 4 °C), resuspended in buffer B (25 mM Tris-HCl, pH 7.4, 300 mM NaCl and 10% glycerol), flash frozen in liquid nitrogen and stored at −80 °C. To purify ASCT2, an aliquot of membrane vesicles representing ~1.5 g cells was solubilized in buffer C (25 mM Tris-HCl, pH 7.4, 300 mM NaCl, 10% (vol/vol) glycerol, 1 mM L-glutamine (Sigma-Aldrich), 1% DDM and 0.1% CHS (Anatrace)) for 1 h at 4 °C. Unsolubilized material was removed by ultracentrifugation (30 min, 442,907 *g*, 4 °C), and 50 mM imidazole, pH 7.4, was added to the supernatant. Subsequently Ni^{2+}–Sepharose resin, preequilibrated with buffer D (20 mM Tris-HCl, pH 7.4, 300 mM NaCl, 50 mM imidazole, pH 7.4, 10% glycerol, 1 mM L-glutamine, 0.05% DDM and 0.005% CHS), was added, and the suspension was incubated for 1 h at 4 °C. The resin was poured into a disposable column, and after unbound material was allowed to flow through, the column was washed with buffer D, and protein was eluted with buffer E (20 mM Tris-HCl, pH 7.4, 300 mM NaCl, 500 mM imidazole, pH 7.4, 10% glycerol, 1 mM L-glutamine, 0.05% DDM and 0.005% CHS). 5 mM Na-EDTA was added to the peak elution fraction, which then was applied to size-exclusion chromatography with a Superdex 200 10/300 gel-filtration column (GE Healthcare) preequilibrated with buffer F (20 mM Tris-HCl, pH 7.4, 300 mM NaCl, 1 mM L-glutamine, 0.05% DDM and 0.005% CHS). Fractions containing purified protein were collected and immediately used for preparing cryo-EM grids or reconstitution into proteoliposomes.

Reconstitution into proteoliposomes. Freshly purified ASCT2 was reconstituted into proteoliposomes, according to the protocol described in ref. [43]. A mixture of *Escherichia coli* polar lipids (Avanti Polar Lipids) and egg phosphatidylcholine (Avanti Polar Lipids) in a ratio of 3:1 (wt/wt) was extruded through a 400-nm-diameter polycarbonate filter (Avestin, 11 passages), then diluted to 4 mg ml^{-1} with buffer G (20 mM Tris, pH 7.0) and destabilized with 10% Triton X-100. ASCT2 was added to the destabilized lipid mixture to a final ratio of 1:250 (wt/wt, ASCT2/lipids). In the indicated experiments 5% (wt/wt) or 10% (wt/wt) cholesterol (Avanti polar lipids) was added to the mixture of *E. coli* polar lipids and egg phosphatidylcholine (3:1 (wt/wt)). After incubation for 30 min at room temperature with gentle rocking, detergent was removed by addition of Bio-beads in four steps: 25 mg ml^{-1} for 30 min at room temperature, 15 mg ml^{-1} for 1 h at 4 °C, 19 mg ml^{-1} with overnight incubation at 4 °C and 29 mg ml^{-1} for 2 h on the next morning at 4 °C. Proteoliposomes were collected by ultracentrifugation (45 min, 442,907 *g*, 4 °C) and resuspended in buffer G to a final lipid concentration of 20 mg ml^{-1}. Proteoliposomes were then divided into aliquots, flash frozen in liquid nitrogen and stored in liquid nitrogen.

Transport assays. Proteoliposomes were resuspended in buffer of the desired lumenal composition, subjected to three freeze–thaw cycles and extruded through a 400-nm-diameter polycarbonate filter (Avestin, 11 passages). The liposomes were then diluted in buffer G and ultracentrifuged (45 min, 442,907 *g*, 4 °C) to remove external substrate. Substrate-loaded proteoliposomes were resuspended in buffer G to a concentration of 10 µg protein per 540 µl. Transport assays were performed at 25 °C with continuous stirring. To start the transport reaction, 60 µl of tenfold-concentrated outside-buffer substrate was diluted in 540 µl of proteoliposomes to reach a final concentration of [^{3}H]L-glutamine (PerkinElmer) of 50 µM. At each indicated time point, 80 µl of proteoliposomes was taken, immediately diluted in 2 ml of cold buffer G (stop buffer), rapidly filtered over a 0.45-µm-pore-size filter (Protran BA-85, Whatman) and washed with 2 ml of the same stop buffer. The filter was dissolved in 2 ml of scintillation liquid (Emulsifier Scintillator Plus, PerkinElmer). The radioactivity was counted with a PerkinElmer Tri-Carb 2800RT liquid scintillation counter.

For experiments in which radiolabeled glutamine was exchanged against different amino acids in the liposomes, the lumen was loaded with 10 mM of the indicated amino acid (or without any amino acid) and with 50 mM NaCl. The outside buffer contained 50 mM NaCl and 50 µM [^{3}H]L-glutamine. For competition experiments, the outside buffer was additionally supplemented with 1 mM of the indicated unlabeled amino acid.

For experiments in which the electrogenic nature of the exchange reaction was assayed, proteoliposomes were loaded with 10 mM L-glutamine and 50 mM KCl. The outside buffer contained 50 mM NaCl, 0.5 mM KCl and 50 µM [^{3}H]L-glutamine, as well as valinomycin (3 µM final concentration) or ethanol as indicated. As a negative control in the absence of sodium, 50 mM KCl and 50 µM [^{3}H]L-glutamine were used on the outside.

For experiments in proteoliposomes containing cholesterol (5% (wt/wt) and 10% (wt/wt)), the lumen was loaded with 50 mM NaCl and 10 mM L-glutamine. The outside buffer included 50 µM [^{3}H]L-glutamine and 50 mM NaCl. A first-order rate equation was used to fit experimental data. Error bars represent s.e.m. from three independent experiments.

For determination of the K_m for Na^+, proteoliposomes were loaded with 10 mM L-glutamine and 300 mM choline chloride. The outside buffer contained a mixture of choline chloride and sodium chloride (cumulative concentration 300 mM), and 50 µM [^{3}H]L-glutamine. For determination of the K_m for glutamine, proteoliposomes, containing 10% (wt/wt) cholesterol were loaded with 10 mM L-glutamine and 50 mM NaCl. The outside buffer included 50 mM NaCl and the indicated [^{3}H]L-glutamine concentration. Initial rates were measured at time points 15 s and 2 min 15 s. The Michaelis–Menten equation was used to fit the data. Error bars represent s.e.m. from three independent experiments, each performed in duplicate.

Cryo-EM sample preparation and imaging. Freshly purified protein was concentrated with Vivaspin concentrating devices with a molecular-weight cutoff of 100 kDa (Sartorius) to 2–2.5 mg ml^{-1}. Then 2.8 µl was applied on holey-carbon cryo-EM grids (Quantifoil Au R1.2/1.3, 200 and 300 mesh), which had previously been glow discharged at 5 mA for 20 s. Grids were blotted for 3–5 s in a Vitrobot (Mark 3, Thermo Fisher) at 20 °C temperature and 100% humidity, subsequently plunge frozen in liquid ethane and stored in liquid nitrogen. Cryo-EM data were collected on a 200-keV Talos Arctica microscope (Thermo Fisher) with a postcolumn energy filter (Gatan) in zero-loss mode, with a 20-eV slit and a 100-µm objective aperture, in an automated fashion with EPU software (Thermo Fisher) on a K2 summit detector (Gatan) in counting mode. Cryo-EM images were acquired at a pixel size of 1.012 Å (calibrated magnification of 49,407×), a defocus range from −0.4 to −2.5 µm, an exposure time of 9 s and a subframe exposure time of 150 ms (60 frames), and a total electron dose on the specimen level of approximately 52 electrons/Å^2. The best regions on the grid were screened with a self-written script to calculate the ice thickness, and data quality was monitored in real time with the software FOCUS[44].

Image processing. A total of 6,345 dose-fractionated cryo-EM images were recorded and subjected to motion correction and dose weighting of frames in MotionCor2 (ref. [45]). The CTF parameters were estimated on the movie frames with ctffind4.1 (ref. [16]). Bad images showing contamination, a defocus below or above −0.4 and −3 µm, or a bad CTF estimation were discarded, thus resulting in 4,863 images used for further analysis with the software package RELION2.1 (ref. [47]). Approximately 3,000 particles were picked manually to generate 2D references, which were improved in several rounds of autopicking. A low threshold was used during the final autopicking step to ensure that no particles were missed, thus yielding more than one million particles. Particles were extracted with a box size of 240 pixels, and initial classification steps were performed with threefold-binned data. False positives or 'bad' particles were removed in the first rounds of 2D classification, thus resulting in 628,015 particles that were further sorted in several rounds of 3D classification. A map generated from the Glt_{Ph} structure (PDB 3KBC) was used as a reference for the first round, and the best output class was used in subsequent jobs in an iterative manner. The best 3D class, comprising 184,080 particles from 4859 images, was subjected to autorefinement, thus yielding a map with a resolution of 4.26 Å before masking and 3.91 Å after masking. Particles were further polished in RELION version 2.1 and subjected to another round of 2D and 3D classification, thus resulting in a final dataset of 133,437 particles. The final polished map had a resolution of 4.26 Å before masking and 3.85 Å after masking. The map was sharpened with an isotropic *B* factor of −171 Å^2; for manual inspection, a *B* factor of −225 Å^2 was used. The approach of focused refinement, wherein the less resolved detergent micelle was subtracted from the particle images, did not improve the resolution (ref. [48]). During 3D classification and autorefinement jobs, *C*3 symmetry was imposed. To check for conformational heterogeneity of the data, in which single protomers within the trimer might adopt a different conformation, 3D classifications with no symmetry imposed were performed at different stages of image processing. We further performed 3D classification on the individual protomers of a single transporter with symmetry expansion and signal subtraction. Both approaches showed no indication of the existence of a different conformation. Local resolution estimates were determined in RELION. All resolutions were estimated with the 0.143 cutoff criterion (ref. [49]) with gold-standard Fourier-shell correlation (FSC) between two independently refined half maps (ref. [50]). During postprocessing, high-resolution noise substitution was used to correct for convolution effects of real-space masking on the FSC curve (ref. [51]).

Model building. The obtained cryo-EM map was used for manual model building in COOT[52] with the previously published structures of EAAT1 (ref. [25]) and Glt_{Tk} (ref. [23]) as references. The resolution of the map was sufficient to unambiguously assign the protein sequence and model most of the side chains with confidence, except for the protruding loop in TM4. Rounds of real-space refinement were performed in Phenix[53] and included a simulated annealing protocol and NCS restraints. Coordinates were manually edited in COOT after each refinement cycle

and subjected to further rounds of refinement. The final validation check was performed with MolProbity (ref. [54]) (Table 1). For validation of the refinement, FSCs (FSC_{sum}) between the refined model and the final map were determined. To monitor the effects of potential overfitting, random shifts (up to 0.5 Å) were introduced into the coordinates of the final model, and this was followed by refinement against the first unfiltered half map. The FSC between this shaken–refined model and the first half map used during validation refinement is termed FSC_{work}, and the FSC against the second half map, which was not used at any point during refinement, is termed FSC_{free}. The marginal gap between the curves describing FSC_{work} and FSC_{free} indicates no overfitting of the model (Supplementary Fig. 1h). Interfaces were calculated with jsPISA (ref. [55]). Images were prepared with the open source version of PyMOL (https://sourceforge.net/projects/pymol/), and videos were made with Chimera (https://www.cgl.ucsf.edu/chimera/).

Reporting Summary. Further information on experimental design is available in the Nature Research Reporting Summary linked to this article.

Data availability. The three-dimensional cryo-EM density maps of the human amino acid exchanger ASCT2 have been deposited in the Electron Microscopy Data Bank under accession number EMD-4386. The deposition includes corresponding maps calculated with higher *B* factors, both half maps and the mask used for the final FSC calculation. Coordinates for the ASCT2 inward-facing model have been deposited in the Protein Data Bank under accession number PDB 6GCT. All other data are available from the corresponding authors upon reasonable request.

References

43. Geertsma, E. R., Nik Mahmood, N. A. B., Schuurman-Wolters, G. K. & Poolman, B. Membrane reconstitution of ABC transporters and assays of translocator function. *Nat. Protoc.* **3**, 256–266 (2008).
44. Biyani, N. et al. The interface between data collection and data processing in cryo-EM. *J. Struct. Biol.* **198**, 124–133 (2017).
45. Zheng, S. Q. et al. MotionCor2: anisotropic correction of beam-induced motion for improved cryo-electron microscopy. *Nat. Methods* **14**, 331–332 (2017).
46. Rohou, A. & Grigorieff, N. CTFFIND4: fast and accurate defocus estimation from electron micrographs. *J. Struct. Biol.* **192**, 216–221 (2015).
47. Kimanius, D., Forsberg, B. O., Scheres, S. H. & Lindahl, E. Accelerated cryo-EM structure determination with parallelisation using GPUs in RELION-2. *eLife* **5**, e18722 (2016).
48. Bai, X.-C., Rajendra, E., Yang, G., Shi, Y. & Scheres, S. H. W. Sampling the conformational space of the catalytic subunit of human γ-secretase. *eLife* **4**, e11182 (2015).
49. Rosenthal, P. B. & Henderson, R. Optimal determination of particle orientation, absolute hand, and contrast loss in single-particle electron cryomicroscopy. *J. Mol. Biol.* **333**, 721–745 (2003).
50. Scheres, S. H. W. & Chen, S. Prevention of overfitting in cryo-EM structure determination. *Nat. Methods* **9**, 853–854 (2012).
51. Chen, S. et al. High-resolution noise substitution to measure overfitting and validate resolution in 3D structure determination by single particle electron cryomicroscopy. *Ultramicroscopy* **135**, 24–35 (2013).
52. Emsley, P. & Cowtan, K. Coot: model-building tools for molecular graphics. *Acta Crystallogr. D Biol. Crystallogr.* **60**, 2126–2132 (2004).
53. Adams, P. D. et al. PHENIX: a comprehensive Python-based system for macromolecular structure solution. *Acta Crystallogr. D Biol. Crystallogr.* **66**, 213–221 (2010).
54. Chen, V. B. et al. MolProbity: all-atom structure validation for macromolecular crystallography. *Acta Crystallogr. D Biol. Crystallogr.* **66**, 12–21 (2010).
55. Krissinel, E. Stock-based detection of protein oligomeric states in jsPISA. *Nucleic Acids Res.* **43**, W314–W319 (2015). W1.